Journal of Fluids and Structures 86 (2019) 200–212

Contents lists available at ScienceDirect

Journal of Fluids and Structures

journal homepage: www.elsevier.com/locate/jfs

The effect of mass ratio on the structural response of a freely vibrating square cylinder oriented at different angles of attack

Jisheng Zhao [a,*], Justin Leontini [b], David Lo Jacono [c], John Sheridan [a]

[a] Fluids Laboratory for Aeronautical and Industrial Research (FLAIR), Department of Mechanical and Aerospace Engineering, Monash University, Victoria 3800, Australia
[b] Department of Mechanical Engineering and Product Design Engineering, Swinburne University of Technology, Hawthorn, Victoria 3122, Australia
[c] Institut de Mécanique des Fluides de Toulouse (IMFT), Université de Toulouse, CNRS, Toulouse, France

ARTICLE INFO

Article history:
Received 28 August 2018
Received in revised form 30 January 2019
Accepted 4 February 2019
Available online 28 February 2019

Keywords:
Fluid–structure interaction
Flow-induced vibration
Square cylinder

ABSTRACT

This study reports on an experimental investigation of the effect of mass ratio on the transverse flow-induced vibration (FIV) response of an elastically mounted square cylinder placed at three different incidence angles: two symmetric with respect to the centreplane, $\alpha = 0°$ and $45°$; and one asymmetric at $20°$. These three angles display different dominant FIV phenomena: transverse galloping and combined vortex-induced vibration (VIV) and galloping for $\alpha = 0°$, VIV for $\alpha = 45°$, and *higher branch* subharmonic (period-doubled) VIV for $\alpha = 20°$ (Nemes et al., 2012). The mass ratio is defined as the ratio of the total oscillating mass (m) to the displaced fluid mass (m_d), $m^* = m/m_d$. The present results show that the mass ratio ($m^* = 2.64$ – 15.00) has a significant influence on the structural vibration response for all FIV phenomena, and can dictate whether two of these modes exist at all. Three primary observations are presented: for the $\alpha = 0°$ case, the combined VIV–galloping response is diminished as the mass ratio is increased, and it ceases to exist for $m^* \geqslant 11.31$; for the $\alpha = 45°$ case, the peak values of the normalised oscillation amplitude during VIV are only reduced marginally with increasing m^*, however the body oscillation amplitude in the desynchronised regions is significantly attenuated; for the $\alpha = 20°$ case, there exists a critical mass ratio ($m^*_{crit} \simeq 3.50$) above which the higher branch subharmonic VIV does not persist.

1. Introduction

Flow-induced vibration (FIV) of bluff bodies has motivated a significant amount of research in the past half-century, due to its importance in a large variety of engineering applications, such as oil risers and offshore structures in ocean currents, wind turbine towers, bridges and high-rise buildings in winds. There are two phenomena typical of FIV of bluff elongated structures in cross-flow: *vortex-induced vibration* (VIV) and *galloping* (see Blevins, 1990; Naudascher and Rockwell, 2005). Fundamentally, VIV is caused by the vortex shedding into the wake of a body, which in turn exerts fluctuating forcing on the structure, causing it to vibrate at a primary frequency similar to that of the vortex shedding. Since the pioneering experiments by Brooks (1960), a circular cylinder with a single degree of freedom (SDOF or 1-DOF) constrained to oscillate transversely in a free stream has been adopted as the idealised model for fundamental research on VIV (e.g. Feng, 1968; Williamson and Roshko, 1988; Khalak and Williamson, 1996; Govardhan and Williamson, 2000; Carberry et al., 2001; Klamo et al., 2005;

* Corresponding author.
E-mail address: jisheng.zhao@monash.edu (J. Zhao).

https://doi.org/10.1016/j.jfluidstructs.2019.02.008
0889-9746/

Leontini et al., 2006; Zhao et al., 2014a). One reason for this is its axial symmetry that prohibits the influence of other forms of FIV. On the other hand, structures with axial *asymmetry* (e.g. a square cross-sectional cylinder) may be susceptible to *transverse galloping*, as opposed to, or in addition to, VIV. Fundamentally, galloping is caused by the asymmetric long-time aerodynamic force arising from the body motion in a fluid flow and so typically occurs at a frequency much less than the vortex shedding. It should be noted that galloping is not the only aeroelastic instability possible — for example, flutter can also occur for the combined plunge-pitch instability of airfoil structures (see Blevins, 1990). Galloping is thus categorised as *movement-induced excitation* (MIE), whereas VIV in caused by the vortex shedding in the wake of a body and thus is categorised as *instability-induced excitation* (IIE) (see Naudascher and Rockwell, 2005). These FIV phenomena are of great practical concern, due to their potential leading to undesired vibration, fatigue damage of structures or even structural failures (e.g. the Tacoma Narrows Bridge collapse in 1940). Comprehensive reviews of previous extensive research on FIV have been given by Bearman (1984), Sarpkaya (2004), Williamson and Govardhan (2004) and books by Blevins (1990), Naudascher and Rockwell (2005), Païdoussis et al. (2010), among others.

Previous studies have shown that the mass ratio, defined as the ratio of the total mass of the oscillating system (m) to the mass of the displaced fluid (m_d), namely $m^* = m/m_\mathrm{d}$, is an important parameter affecting the FIV response of a system. For the circular cylinder, a comparison of high mass ratio wind tunnel experiments with $m^* = O(100)$ by Feng (1968), to a series of studies by Khalak and Williamson (1996, 1997a,b, 1999) of a hydro-elastic system with low mass ratio ($m^* = O(1)$) shows that the low-mass-ratio system exhibits a much wider *"lock-in"* region and substantially larger oscillations (with the peak amplitude up to one diameter of the body). The low-mass-ratio system also has three (the *"initial"*, *"upper"* and *"lower"*, as named by Khalak and Williamson (1996, 1997a,b, 1999)) branches and a desynchronised region as a function of the reduced velocity. Note that the reduced velocity is defined by $U^* = U/(f_\mathrm{n}H)$, where U is the free-stream velocity, f_n is the natural frequency of the system in quiescent fluid, and H is the frontal projected width of the body (e.g. the cylinder diameter D).

A critical mass ratio also appears to exist, below which the cylinder exhibits large amplitude oscillations at a frequency near the Strouhal frequency regardless of U^*. This critical mass is typically $m^*_\mathrm{crit} \leqslant 0.54$, but the exact value is Reynolds number (Re) dependent (see Govardhan and Williamson, 2002; Branković, 2004; Ryan et al., 2005). Note that the Strouhal frequency, denoted by f_St in this study, refers to the vortex shedding frequency of the stationary body, and its normalised form, the Strouhal number, is defined by $\mathrm{St} = f_\mathrm{St}H/U$; the Reynolds number is defined by $Re = UH/\nu$, where ν is the kinematic viscosity of the fluid. Clearly, the mass ratio has a significant, and non-trivial, influence on the VIV response.

Although there have been a considerable amount of studies conducted on FIV of a square cylinder that has been widely adopted as the canonical model for transverse galloping, little attention has been paid to the effect of mass ratio in this problem. Following the pioneering study of Den Hartog (1932) who first proposed a criterion for the onset of galloping of ice-coated cables in winds, Parkinson and Smith (1964) developed a quasi-steady theory to predict the amplitude response of a square cylinder undergoing galloping. In general, this quasi-steady theory has been successfully implemented in aeroelastic systems with relatively high mass and damping ratios, where the galloping oscillation frequency is much lower than the vortex shedding frequency. With a low-damping system in wind tunnel experiments, Bearman et al. (1987) observed that, while the amplitude response could be generally predicted using the quasi-steady theory of Parkinson and Smith (1964), a "kink" region in the amplitude response occurred at $U^* \approx 6\pi$, with a noticeable third-harmonic frequency of the body vibration present in the frequency components of the transverse lift. This indicates that in some circumstances galloping is still affected by the vortex shedding. Luo and Bearman (1990) noted that the quasi-steady theory of galloping was able to predict the fluctuating lift on a transversely oscillating square cylinder at high reduced velocity, but not at intermediate to low reduced velocity, due to the influence of vortex shedding and fluid inertia forces. Theoretical analysis of the effect of the vortex shedding on the galloping response was performed by Bokaian and Geoola (1984). Later, Corless and Parkinson (1988, 1993) proposed a model for the combined effects of VIV and galloping. These attempts, however, had limited success.

The experimental investigation on the influence of angle of attack (α) of a square cylinder with low mass ratio ($m^* = 2.2$) from Nemes et al. (2012) identified three α regimes; one dominated by galloping at low angles of attack $0^\circ \leqslant \alpha \lesssim 7.5^\circ$, a second with combined VIV–galloping at medium angles of attack $10^\circ \lesssim \alpha \leqslant 22.5^\circ$, and a third dominated by VIV at high angles of attack $25^\circ \leqslant \alpha \leqslant 45^\circ$. They observed a new *higher branch (HB)* over the medium α range, where the body oscillation amplitudes are significantly larger than those seen in the upper branch associated with pure VIV, but with a oscillation frequency component locked onto approximately the first subharmonic of the Strouhal frequency, $f_\mathrm{St}/2$. Subsequently, Zhao et al. (2014b) conducted an in-depth investigation for three representative cases $\alpha = 0^\circ$, 20° and 45°, employing accurate force measurements and flow visualisations based on particle image velometry (PIV) measurements, and revealed that: the $\alpha = 0^\circ$ case exhibited odd-integer (i.e. 1:1, 1:3, 1:5) synchronisations between the galloping frequency and the vortex shedding frequency; the $\alpha = 45^\circ$ case in general was characterised by VIV response but comprised of a number of distinctly different regimes; the $\alpha = 20^\circ$ case underwent a transition from a typical VIV *upper branch* to a *higher branch*, which was associated with a change in the wake from a 2S mode to a 2(2S) mode. More recently, Zhao et al. (2018c.) provided a further analysis using continuous wavelet transforms and recurrence plots on the dynamical states associated with synchronisation regimes at the aforementioned three α values.

While most of the previous studies of FIV of a square cylinder have been conducted with high mass ratio at zero angle of attack (e.g. Parkinson and Smith, 1964; Bearman et al., 1987; Amandolèse and Hémon, 2010; Manzoor et al., 2010; Sheikh et al., 2014), limited attention has been given to the effect of mass ratio on the FIV response of a square cylinder. Zhao et al. (2013) numerically investigated the VIV of a square cylinder with $m^* = 3$ at $\alpha = 0^\circ$, 22.5° and 45° in a laminar flow at $Re = 100$. Joly et al. (2012) showed that galloping of a square cylinder at low Reynolds numbers only occurred for

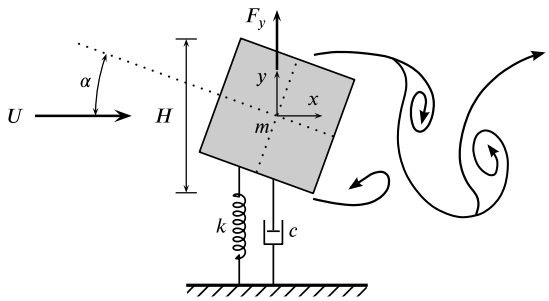

Fig. 1. A definition sketch for FIV of a square cross-sectional cylinder with variable angle of attack α. The square cylinder is allowed to oscillate freely only in the transverse direction y, to the oncoming flow U in the stream-wise direction x. Note that H is the frontal projected length of the cylinder. A square cylinder at $\alpha = 0°$ is referred to as a square orientation, while $\alpha = 45°$ as a "diamond" orientation.

$Re > 140$, and that galloping amplitude decreased abruptly for decreasing m^* values close to 3 at $Re = 200$, whereas Jaiman et al. (2016) observed, at the same Re, that the galloping amplitude decreased as m^* was increased from 0.1 to 1, but then increased as m^* was increased from 3 to 10. In their low-Reynolds-number ($50 \leqslant Re \leqslant 250$) numerical study of a square cylinder ($\alpha = 0°$), Sen and Mittal (2015, 2016) reported that the onset reduced velocity of galloping decreased as m^* was increased. Miyanawala and Jaiman (2018) showed that their numerical results (at $\alpha = 0°$) at subcritical Reynolds numbers agreed generally with the benchmark study of Zhao et al. (2014b), in terms of the amplitude response. Using a computational scheme based of a variational formulation and incorporating a subgrid turbulence model to simulate the fluid–structure interaction, they also predicted the "odd" synchronisation regions and associated wake modes originally observed by Zhao et al. (2014b). However, the effect of mass ratio on the FIV response of a square cylinder at various angles of attack is still largely unknown, particularly for high Reynolds numbers. Thus, the present study aims to extend the previous work of Zhao et al. (2014b) to examine the effect of mass ratio on the structural response of a freely vibrating square cylinder at the three aforementioned representative angles of attack $\alpha = 0°$, 20° and 45°, in a high Re range, where the FIV response is likely to be relatively insensitive to Reynolds number.

While the mass ratio impacts all of the response regimes to some degree, it is shown that three of the previously reported response regimes are most severely impacted. For the $\alpha = 0°$ case, the combined VIV–galloping response is diminished as the mass ratio is increased, and it completely disappears for $m^* \geqslant 11.31-$ this observation quantifies the observation that the VIV and galloping dynamics do not interact when the mass ratio is high and there time scales are well separated. For the $\alpha = 45°$ case, the amplitude of the response during VIV is only marginally reduced, however it is significantly attenuated in the desynchronised region. For the asymmetric $\alpha = 20°$ case, is shown the higher branch subharmonic VIV which produces the largest amplitudes of oscillation only exists below a critical mass ratio of $m^*_{\text{crit}} \simeq 3.50$.

The paper proceeds by describing the experimental details in Section 2. The results and discussion, including the vibration amplitude and frequency responses, and analyses of the fluid forcing and phasing, are presented in Section 3. Finally, conclusions are drawn in Section 4.

2. Experimental method

2.1. Fluid–structure system modelling

A schematic of the transverse FIV of a square cylinder with a variable angle of attack is shown in Fig. 1, which defines key parameters of the system. The elastically mounted cylinder is allowed to oscillate freely in only one direction transverse to the oncoming free stream. The body dynamics are governed by the linear second-order mass–spring–damper oscillator equation:

$$m\ddot{y}(t) + c\dot{y}(t) + ky(t) = F_y(t)\,, \tag{1}$$

where c is the structural damping of the system, k is the spring constant, $y(t)$ is the body displacement, and $F_y(t)$ represents the transverse fluid force (lift).

The present fluid–structure system was modelled using a low-friction air bearing system in conjunction with the free-surface recirculating water channel of the *Fluids Laboratory for Aeronautical and Industrial Research (FLAIR)* at Monash University. This water channel facility has a test section of 4000 mm in length, 600 mm in width and 800 mm in depth. The free-stream velocity in the present experiments was varied continuously in a range of $U = 45$–450 mm s^{-1}, and the free-stream turbulence level was found to be less than 1%. More details of the air bearing system and the water channel facility can be found in Nemes et al. (2012), Zhao et al. (2014a,b).

The rigid square cylinder model used, made from aluminium square cross-sectional tubing, had a side width of 24.6 mm. The immersed length was $L = 620$ mm, giving an aspect ratio range of $17.8 \leqslant AR = L/H \leqslant 25.2$. The displaced mass of water was found to be $m_{\text{d}} = \rho D^2 L/4 = 373.2$ g with ρ the density of water, resulting in a minimum achievable mass

Table 1
The experimental parameters of the total mass, the natural frequencies in both quiescent air and water, and the structural damping ratio for different mass ratios.

m^*	m [g]	m_d [g]	f_{na} [Hz]	f_{nw} [Hz]	ζ
2.64	985.4	373.2	0.803	0.648	2.58×10^{-3}
3.00	1119.6	373.2	0.753	0.618	2.51×10^{-3}
3.50	1306.2	373.2	0.700	0.587	2.46×10^{-3}
3.60	1347.8	373.2	0.669	0.580	2.59×10^{-3}
4.00	1492.8	373.2	0.654	0.557	2.54×10^{-3}
5.00	1866.0	373.2	0.586	0.515	2.46×10^{-3}
7.50	2799.0	373.2	0.656	0.603	1.70×10^{-3}
10.00	3732.0	373.2	0.570	0.530	1.57×10^{-3}
11.31	4220.9	373.2	0.647	0.610	2.69×10^{-3}
15.00	5598.0	373.2	0.565	0.544	1.31×10^{-3}

ratio of $m^* = 2.64$ for the present experiments. The mass ratio was tested in the range of $2.64 \leqslant m^* \leqslant 15.00$, which was varied by adding extra weights on top of the air bearing rig. The natural frequencies in air (f_{na}) and in quiescent water (f_{nw}) were individually measured by conducting free-decay tests. Details of the parametric values of the structural properties ($m^*, m, m_d, f_{na}, f_{nw}, \zeta$, etc.) are given in Table 1, noting that $\zeta = c/(2\sqrt{k(m+m_A)})$ denotes the structural damping ratio with consideration of the added mass $m_A = ((f_{na}/f_{nw})^2 - 1)m$. In order to maintain U^* and Re in similar ranges for different m^* cases, the number of extension spring pairs was also varied depending on the total mass. To reduce end effects of the cylinder and also to promote parallel vortex shedding, an end conditioning platform technique was used (see Khalak and Williamson, 1997a; Zhao et al., 2014a,b; Wong et al., 2017, 2018; Zhao et al., 2018a,b). This platform had a height of 165 mm and a top plate with dimensions of 600 mm × 400 mm × 5 mm. A small gap of approximately 1 mm ($\sim 4\%H$) was set between the cylinder free end and the platform top plate.

2.2. Measurements

The cylinder displacement was measured using a non-contact magnetostrictive linear variable differential transformer (LVDT) that was capable of a measurement range of 250 mm with an accuracy of ±0.01% (or $0.001H$) (see Nemes et al., 2012; Zhao et al., 2014b). Simultaneously with the cylinder displacement, the lift and drag forces acting on the cylinder were measured using a two-component force balance based on sensitive semiconductor strain gauges configured in a full Wheatstone bridge circuit. To recover the transverse lift, the inertia force due to the cylinder's acceleration was taken into account, and thus the instantaneous transverse lift can be determined by

$$F_y = F_{SG} + m_B \ddot{y}_b\,, \tag{2}$$

where F_{SG} is the calibrated force output from the corresponding channel of the strain-gauge force balance, m_B is the bottom part of the system's mass consisting of half the force balance sting and the entire cylinder model, and $\ddot{y}_b$ is the cylinder acceleration. The lift coefficient is defined by $C_y = F_y/(\frac{1}{2}\rho U^2 HL)$ in the present study. The instantaneous relative phase angle between the lift and the body displacement was calculated using the Hilbert transform (see Hahn, 1996). More details of the force measurement technique and validation have been given in Zhao et al. (2014b).

Furthermore, the measurements at each reduced velocity were sampled at 100 Hz for 300 s (for more than 100 body vibration cycles), using a data acquisition system (DAQ) based on a PCI DAQ card (model: PCI-6221, National Instruments, USA) interfaced with customised LabVIEW (National Instruments) programs that were also used to control the flow velocity. Further experimental details of the experimental setup and validation can be found in the study of Zhao et al. (2014b). The reduced velocity range investigated was $3 < U^* < 26$, and the corresponding Reynolds number range was $1000 < Re < 12\,300$.

3. Results and discussion

3.1. The impact of m^* for $\alpha = 0°$

Fig. 2 shows the normalised amplitude response (A^*_{10}) together with the normalised logarithmic-scale power spectral density (PSD) contours of frequency response of the body vibration (f^*_y) as a function of reduced velocity for various mass ratios, $m^* = 2.64$, 5.00, 11.31 and 15.00. Fig. 3 shows the corresponding PSD contours of the transverse lift ($f^*_{C_y}$). The frequency PSD contour plots were constructed by stacking together the power spectra of the time series of the cylinder vibration for each U^* (see Zhao et al., 2014b). As can be seen, all the m^* cases in general exhibit an increasing trend in A^*_{10} increasing with U^* for U^* above some threshold value. This threshold value increases with m^*, i.e. $U^* \approx 3$ for $m^* = 2.64$ and $U^* \approx 4.5$ for $m^* = 15.00$. Of particular interest are the "kink" regions in the amplitude response. As noted in the previous study of Zhao et al. (2014b), for $m^* = 2.64$, the first kink occurs around $U^* = 6$. This small regime is characterised by a VIV response, where the body vibration is highly periodic, with the dominant frequency synchronised with the vortex shedding

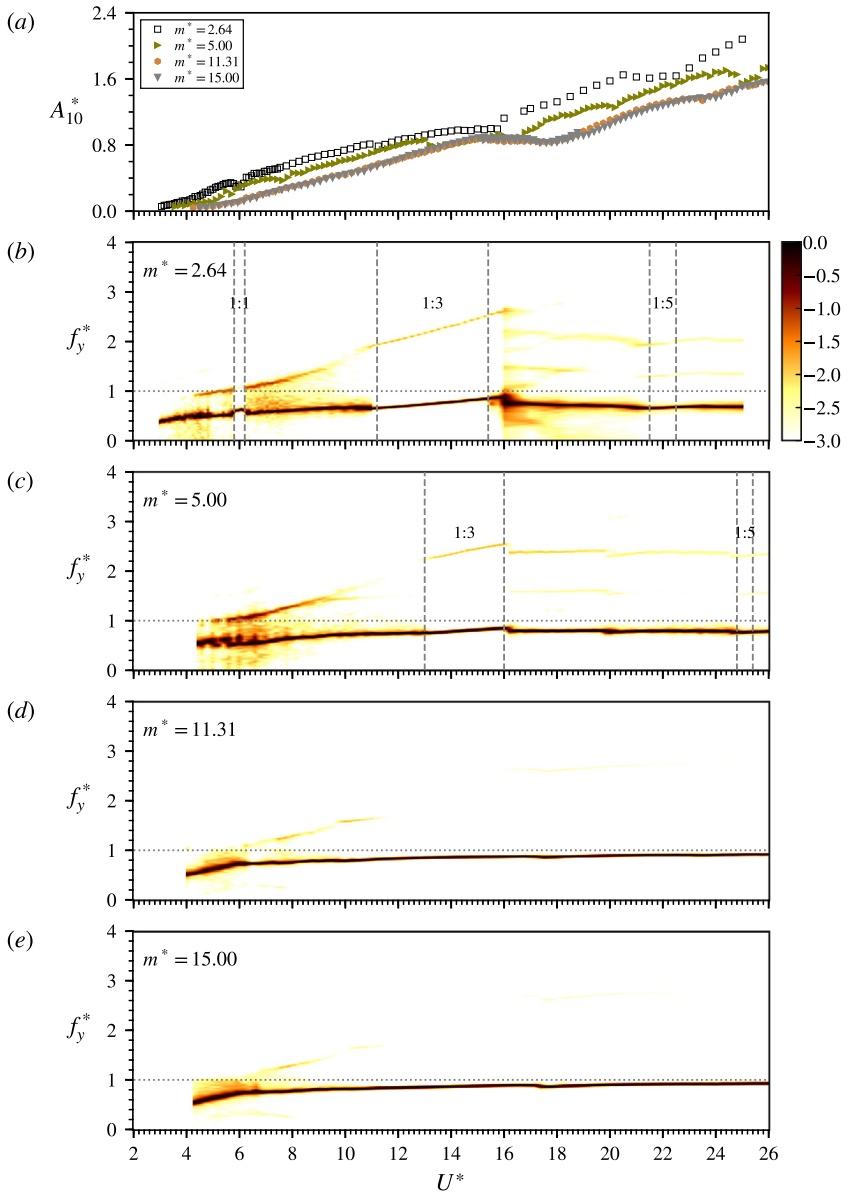

Fig. 2. The normalised amplitude response (*a*) and the logarithmic-scale frequency power spectrum contours (*b*)–(*e*) of the body vibration for $\alpha = 0°$ with various mass ratios. The vertical dashed lines represent boundaries of the "odd" synchronisation regimes. Note that the case of $m^* = 2.64$ is reproduced from Zhao et al. (2014b).

frequency, as in a 1:1 synchronisation. The second kink occurs over a much wider range of $11 \lesssim U^* \lesssim 16$, in which both f_y^* and $f_{C_y}^*$ responses exhibit a third harmonic frequency component, as shown in (*b*) of Figs. 2 and 3. Zhao et al. (2014b) have shown that this is a 1:3 synchronisation associated with a 3(2S) wake mode comprising three cycles of two opposite-signed single vortices shed per body oscillation cycle. Similarly, the third kink with a weak 1:5 synchronisation occurs over a narrow reduced velocity range centred around $U^* = 22$.

While the general trend of classical galloping response is encountered in all the m^* cases (amplitude approximately linearly increasing with flow speed), the amplitude response decreases as the mass ratio is increased. There is also an impact of m^* on the synchronisation regimes. Moving from $m^* = 2.64$ to $m^* = 5.00$ the frequency response in Fig. 2(*c*) shows that the 1:1 synchronisation region disappears, the range of U^* for the 1:3 synchronisation region shrinks to $13 \lesssim U^* \lesssim 16$, and the 1:5 synchronisation also occurs over a noticeably narrower U^* range. Furthermore, the dominant galloping frequency is $f_y^* \approx 0.75$, slightly higher than $f_y^* \approx 0.6$ seen for $m^* = 2.64$. A similar trend is also seen in the $f_{C_y}^*$ response shown in Fig. 3(*c*), but the harmonic frequency components are relatively stronger, indicating that the vortex shedding process is faster than the body vibration.

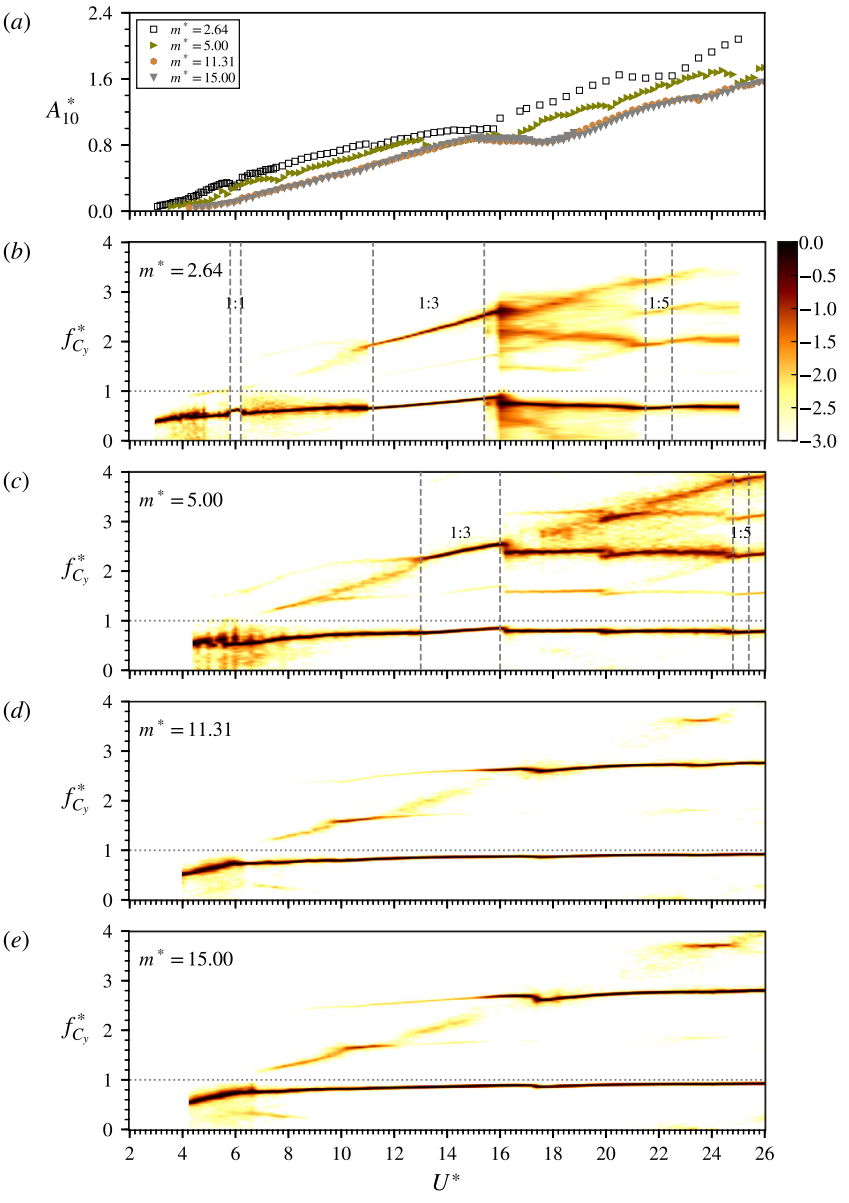

Fig. 3. The normalised amplitude response in (*a*) and the logarithmic-scale PSD contours of the transverse lift frequency ($f^*_{C_y}$) in (*b*)–(*e*) for $\alpha = 0°$ with various mass ratios. Note that the case of $m^* = 2.64$ is reproduced from Zhao et al. (2014b).

For the higher mass ratio cases $m^* = 11.31$ and 15.00, the amplitude responses appear to be almost identical. Although a kink is observed over $15 < U^* < 18$, it is difficult to identify the aforementioned synchronisations from the f^*_y responses in Fig. 2(*d*, *e*). Moreover, the dominant galloping frequency is found to be $f^*_y \approx 0.93$. On the other hand, the $f^*_{C_y}$ responses of these two m^* cases become dominated gradually by a frequency at three times of the galloping frequency for $U^* > 15$, similar to the galloping response of a D-section cylinder for high U^* values reported by Zhao et al. (2018a). These results indicate that, as m^* is increased, the synchronisation regions can be significantly shrunk, and the galloping frequency approaches f_{nw}.

3.2. The impact of m^* for $\alpha = 45°$

Fig. 4 shows the A^*_{10} and f^*_y responses as a function of U^* for the $\alpha = 45°$ case with various mass ratios, $m^* = 2.64$, 3.00, 4.00, 7.50, 10.00 and 15.00. Clearly, all the m^* cases at $\alpha = 45°$ exhibit a VIV response over the entire U^* range tested. As m^* is increased, the region of periodic body oscillations, which is bounded by the vertical dashed lines in the f^*_y response plots, becomes narrower, i.e. from $3 < U^* < 7.5$ for $m^* = 2.64$ to $3.5 < U^* < 6.4$ for $m^* = 15.00$. Moreover, while the A^*_{10}

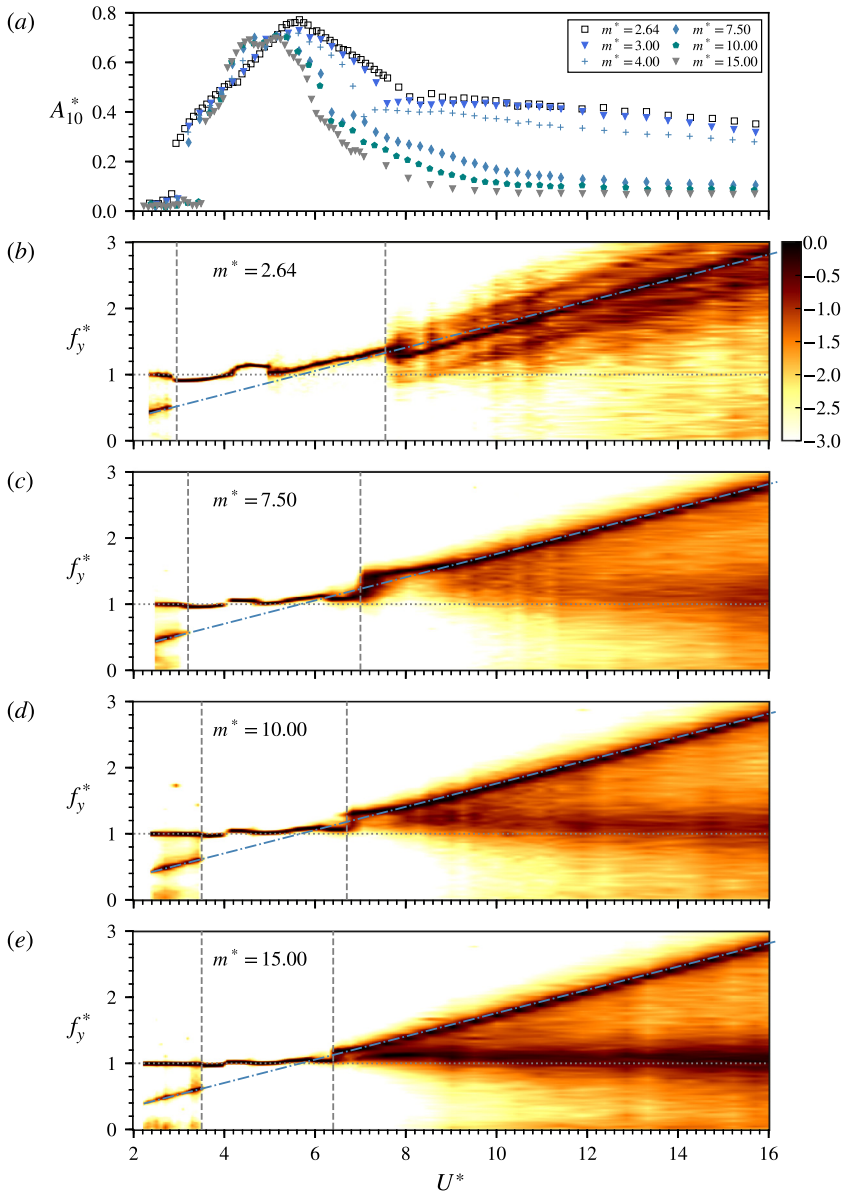

Fig. 4. The A_{10}^* responses as a function of U^* are plotted for the $\alpha = 45$ orientation with various m^* values in (*a*), and the f_y^* responses for selected m^* cases are plotted in (*b*) – (*e*). The vertical dashed lines represent the boundaries of the regions where periodic body oscillations occur. Note that the case of $m^* = 2.64$ is reproduced from Zhao et al. (2014b).

peak tends to decrease slightly, the U^* at which the A_{10}^* peaks also tends to occur at a lower value, i.e. from $A_{10}^* \simeq 0.77$ at $U^* = 5.7$ for $m^* = 2.64$ to $A_{10}^* \simeq 0.70$ at $U^* = 5.1$ for $m^* = 15.00$.

Of further interest is how the A_{10}^* values decrease in the desynchronised regions (the regions beyond the synchronisation regions) for increasing m^*. Compared to the A_{10}^* peak reduction in the synchronisation regions, much larger attenuation is seen in the desynchronisation regions, from $A_{10}^* \approx 0.4$ for $m^* = 2.64$ to $A_{10}^* \approx 0.1$ for $m^* = 15.00$. A representative case of $U^* = 16$ in the desynchronisation region has been chosen to investigate scaling of the amplitude with m^*. As shown in Fig. 5, it seems that A_{10}^* scales with $1/m^*$. Furthermore, as can be seen from Fig. 4($b-e$), while the f_y^* response for a low-m^* system (i.e. $m^* = 2.64$) exhibits the dominant component at the Strouhal frequency ($\mathrm{St} \simeq 0.178$) in this region, despite of the appearance of broadband noise, it exhibits a progressively stronger component close to f_{nw} as m^* is increased. The above results indicate that the mass ratio has a significant effect on the desynchronised region for the diamond orientation.

Fig. 6 shows the root-mean-square (rms) coefficient of the transverse lift (C_y^{rms}), together with the variation of the total phase (ϕ_{total}), as a function of U^* for all the m^* cases at $\alpha = 45°$. Note that the total phase is defined as the relative phase angle between the transverse lift to the body displacement. As shown by Zhao et al. (2014b) that the switch of ϕ_{total} from

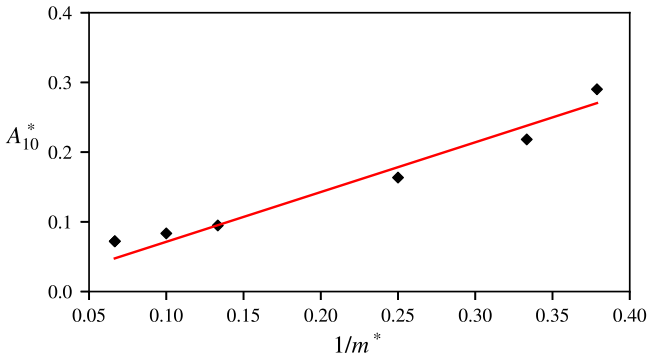

Fig. 5. Variation of A_{10}^* with m^* at $U^* = 16$ in the desynchronisation region for $\alpha = 45°$. The red line represents the linear fitting of A_{10}^* through all the m^* cases.

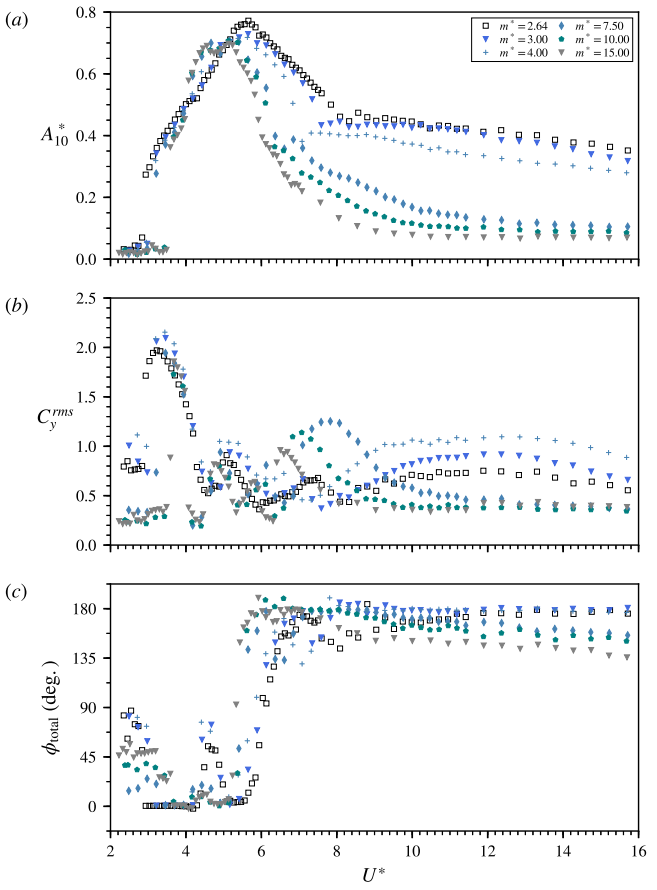

Fig. 6. (a) The A_{10}^* values for the $\alpha = 45°$ case revisited, along with (b) the r.m.s. coefficient of the transverse lift and (c) the total phase as a function of U^* for a series of mass ratios m^*. Note that the case of $m^* = 2.64$ is reproduced from Zhao et al. (2014b).

0° to 180° indicates a transition regime leading to the fluid–structure desynchronisation, it is found that the onset of this transition regime tends to occur at a lower U^* value as m^* is increased. In general, all the m^* cases exhibit similar variation trends in both C_y^{rms} and ϕ_{total}. Since a detailed discussion has been provided by Zhao et al. (2014b) on the five different flow regimes for the case of $m^* = 2.64$, we focus here on the effect of m^* on the fluid forcing C_y^{rms} in the desynchronisation region. Noting that the body vibration amplitude decreases with increasing m^*, there are two trends in the variation of C_y^{rms}: for $m^* \leqslant 4$, C_y^{rms} tends to increase with m^*, while for the cases of $m^* \geqslant 7.5$, C_y^{rms} is almost constant with m^*.

These trends fit with the prediction of a highly idealised force balance. If it is assumed that the vortex shedding exerts a sinusoidal force on the body, it can be shown via Eq. (1) that

$$\frac{A}{F_y} = \left[(k - m\omega^2)^2 + (\omega c)^2\right]^{-1/2} \tag{3}$$

where ω is the angular oscillation frequency. Two conclusions can be drawn from this equation:

- For cases where U^* is large, $k \to 0$, and so the ratio $A/F_y \propto 1/m$. This implies that as m (or equivalently m^* if all other parameters are constant) is increased, the amplitude should decrease and/or the lift coefficient should increase, as is observed for the low m^* cases oscillating at a frequency close to the Strouhal frequency
- For cases where the oscillation frequency is close to the natural frequency, $\omega \simeq \omega_n \simeq \sqrt{k/m}$, and $A/F_y \propto 1/(\omega c)$. Since this is not directly dependent on m or m^*, the amplitude of the oscillation and lift coefficient should be essentially constant with respect to m^*, as is observed for the high m^* cases.

While the argument above is based on a simplified model, the predictions it provides match with measurements. It therefore seems useful to aid in the interpretation of the dynamics.

3.3. The impact of m^* for $\alpha = 20°$

Fig. 7 shows the amplitude A^*_{10} and frequency f^*_y responses, as a function of U^* for various m^* values at $\alpha = 20°$. Two features are immediately apparent. Firstly, there exists a critical value $m^*_{\text{crit}} = 3.5$, above which the higher branch is not encountered. Secondly, the body vibration amplitude is significantly attenuated in the desynchronisation regions as m^* is increased, similar to the diamond orientation case.

The dependence of the higher branch on m^* can be understood when the complex vortex formation and shedding process that occurs for the higher branch, as described by Zhao et al. (2014b), is considered. The associated subharmonic vortex shedding process consists of vorticity production on the rear face, then the lateral faces of the body, to produce the vortices that create the driving force to cause the structural vibration. The body therefore needs to respond quickly to changes in vortex locations and therefore the driving force. This means the vortex shedding mode is sensitive to the instantaneous phase between the generated force and the body motion. Once the body exceeds a given weight, the lag between the generated force and the body motion is too great, and as a result the subharmonic synchronisation cannot be maintained. This can be demonstrated in Fig. 9(c). For $m^* \leqslant 3.5$, the total phase first drops to $\phi_{\text{total}} \simeq 0°$ with the onset of the higher branch, and then increases with U^* before undergoing an abrupt jump to above 90° when the fluid–structure desynchronisation occurs at the end of the higher branch.

In a similar manner, it is perhaps not surprising that the body vibration amplitude in the desynchronisation region quickly reduces with an increase in the mass of the system. With no correlated force to drive the motion, the phase lag between the driving force arising from the vortex shedding process and the body motion is too great for a heavy body to oscillate at any appreciable amplitude. Similar to the diamond orientation case, Fig. 8 demonstrates that the vibration amplitude scales with $1/m^*$ at a representative reduced velocity, $U^* = 16$, for this α case.

It can be seen from Fig. 9 that both C_y^{rms} and ϕ_{total} collapse in the upper branch (e.g. occurring in the range of $4.4 \lesssim U^* \lesssim 6.4$) for all the m^* cases, suggesting that the fluid forcing is essentially insensitive to m^* in this branch, despite some dependence of the vibration amplitude on m^*.

Similar to the $\alpha = 45°$ case, C_y^{rms} tends to increase with m^* for $m^* \leqslant 4$ in the desynchronisation region, while it is close to constant with respect to m^* for $m^* \geqslant 7.5$.

3.4. An overview of the impact of m^* on the A^*_{10} response for $\alpha = 0°$, $20°$ and $45°$

To summarise the impact of m^* on the vibration amplitude response, Fig. 10 shows an overview of the A^*_{10} contours as a function of U^* and m^* for the three incidence angles, $\alpha = 0°$, $20°$ and $45°$. As can be seen in the $\alpha = 0°$ case, the "odd" (1:1, 1:3 and 1:5) synchronisation regions, which are a combined VIV–galloping response, only occur at m^* lower than certain values, while the global growth of the galloping oscillation amplitude persists as U^* is increased, despite changes in m^*. This quantifies the previous observations that galloping and VIV do not interact when the mass ratio is high and the time scales of the two oscillations are well separated — the measurements summarised in Fig. 10 indicate $m^* \geqslant 11.31$ will ensure the two modes do not interact. For the case of $\alpha = 20°$, the VIV lock-in (1:1) region, occurring over the reduced velocity range of $4.5 \lesssim U^* \lesssim 6.3$ (bounded by dashed lines), appears to be very robust over the m^* range tested; however, the higher branch (HB) region, which leads to even higher amplitudes of oscillation, exists only at $m^* \leqslant 3.50$ over the reduced velocity range of $7.9 \lesssim U^* \lesssim 9.4$; moreover, outside of the regions of the 1:1 VIV lock-in and the higher branch, the A^*_{10} response decreases rapidly towards a stable region for $U^* > 7.5$ and $m^* > 5$. For the VIV case of $\alpha = 45°$, the A^*_{10} contours in both the 1:1 lock-in and desynchronisation regions appear to be very similar to those of the $\alpha = 20°$, while its lock-in region tends to shrink slightly with increasing m^*.

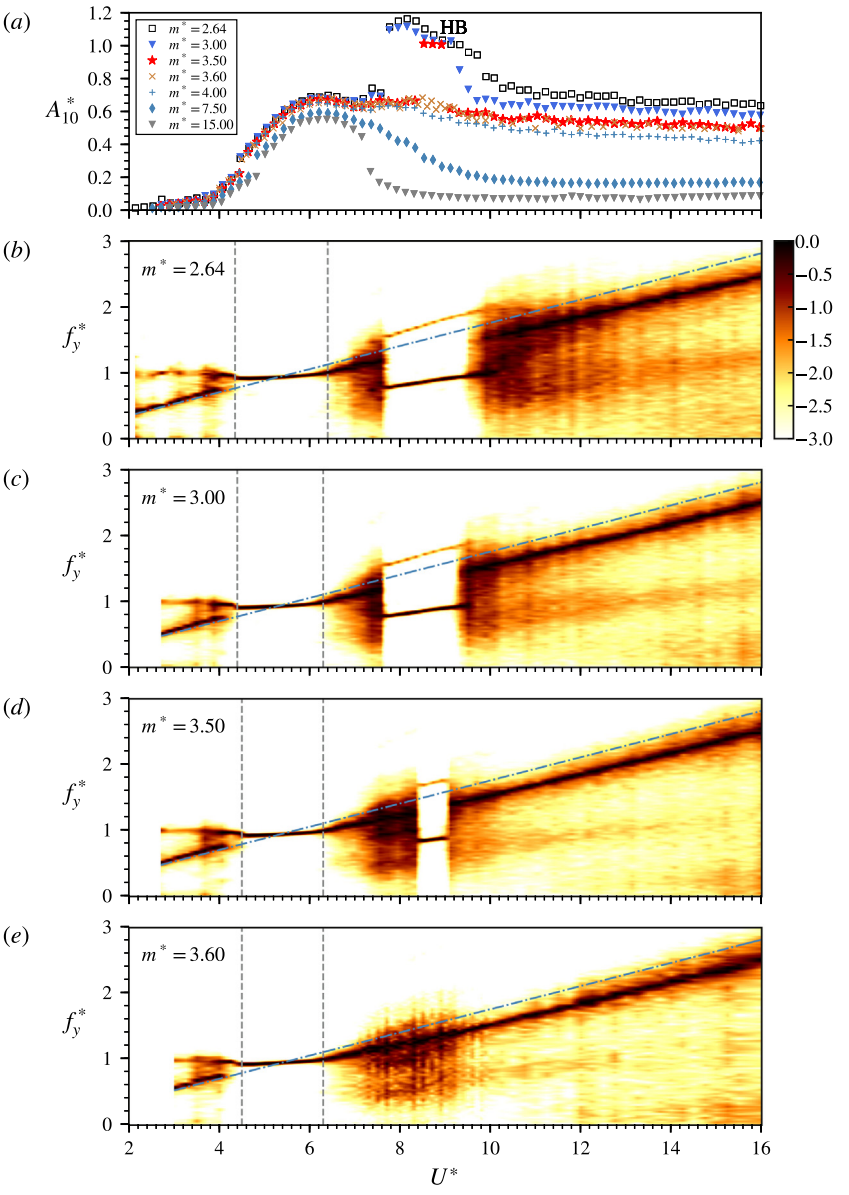

Fig. 7. The A_{10}^* and f_y^* responses showing the existence of a critical mass ratio of $m_{\text{crit}}^* = 3.50$ for the presence of the higher branch is observed for the $\alpha = 20°$ orientation. Note that (*b*) – (*e*) present the selected f_y^* responses of $m^* = 2.64$, 3.0, 3.50, and 3.60, respectively. The vertical dashed lines represent the boundaries of the 1:1 VIV synchronisation region.

4. Conclusions

The effect of mass ratio on the transverse FIV response of an elastically mounted square cylinder has been experimentally investigated for three representative angles of attack, $\alpha = 0°$, 20° and 45°, in the reduced velocity range of $3 < U^* < 25$.

For $\alpha = 0°$, all the m^* cases exhibited a galloping response at high U^* values. However, it was found that, as the mass ratio was increased, the "odd" synchronisation regions shrunk significantly and even diminished, i.e. the 1:1 synchronisation disappeared at $m^* = 5$, while the 1:3 synchronisation became difficult to identify at $m^* = 11.31$. On the other hand, significant influence of m^* was also observed on the galloping frequency, which tended to approach f_{nw} with increasing m^*. Moreover, the onset U^* for the occurrence of significant body oscillations increased with m^*. In general, the FIV response at high mass ratios (i.e. $m^* = 11.31$ and 15.00) is consistent with the classical galloping response previously reported in the literature.

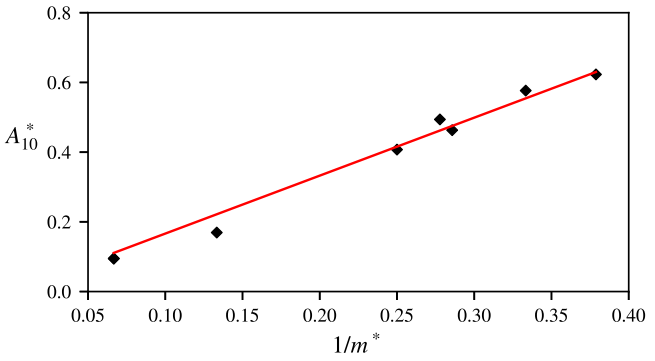

Fig. 8. Variation of A_{10}^* with m^* at $U^* = 16$ in the desynchronisation region for $\alpha = 20°$. For more details, see the caption of Fig. 5.

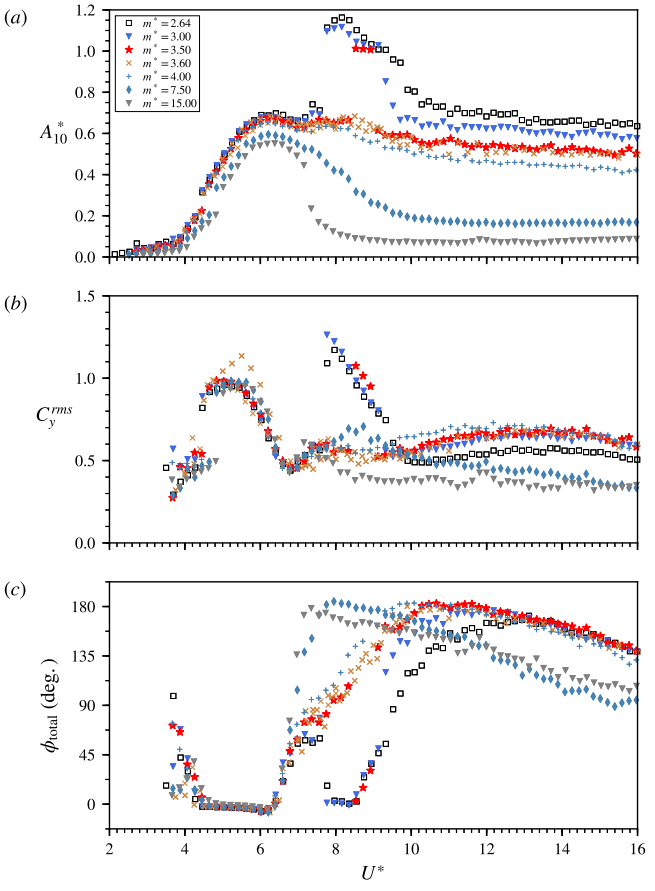

Fig. 9. (a) The A_{10}^* values for the $\alpha = 20°$ case revisited, along with (b) the r.m.s. coefficient of the transverse lift and (c) the total phase as a function of U^* for a series of mass ratios m^*. Note that the case of $m^* = 2.64$ is reproduced from Zhao et al. (2014b).

For $\alpha = 45°$, the largest impact of m^* was found on the vibration response in the desynchronisation region, where significant attenuation was observed in the A_{10}^* response with increasing m^*. It was showed that A_{10}^* scaled with $1/m^*$ for a given U^* in the desynchronisation region.

For $\alpha = 20°$, two striking features were observed that could be associated with the influence of m^*. First, there existed a critical mass of $m_{crit}^* = 3.50$, below which the higher branch was observed. Second, similar to the $\alpha = 45°$ case, the mass ratio also had a significant reduction effect on the vibration amplitude response in the desynchronisation region, with A_{10}^* scaling with $1/m^*$. The findings suggest that these effects of m^* on the higher branch and the desynchronised region are associated with a phase lag between the fluid forcing and the body motion.

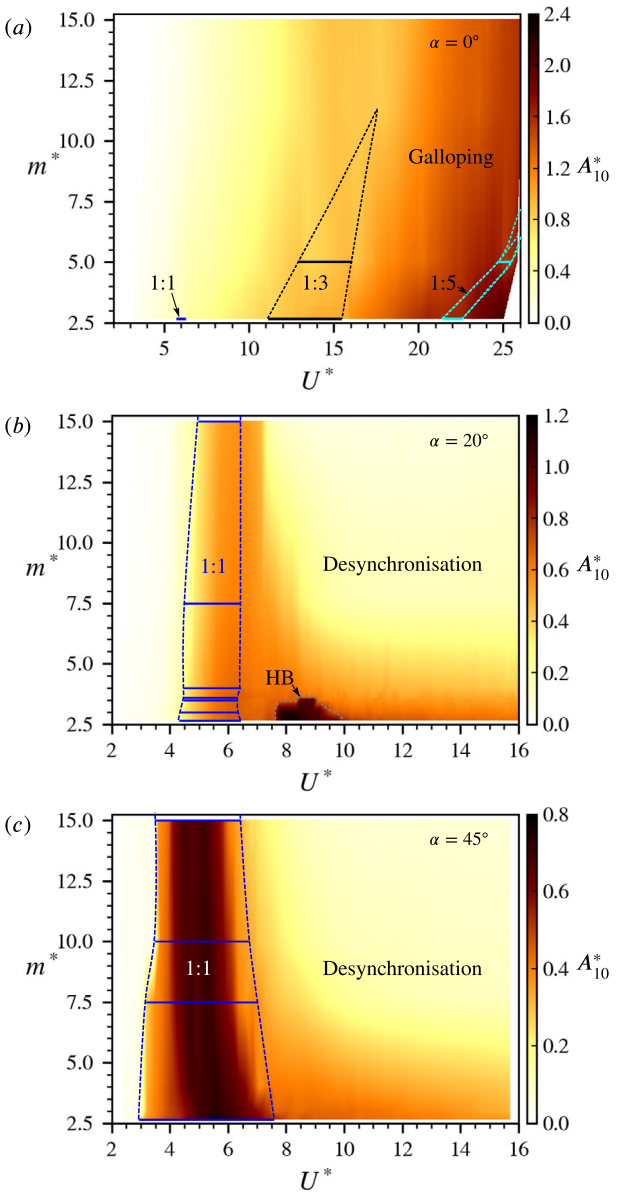

Fig. 10. The A^*_{10} contours are plotted as a function of U^* and m^* for (*a*) $\alpha = 0°$, (*b*) $\alpha = 20°$ and (*c*) $\alpha = 45°$. Note that the dashed lines represent the boundaries of synchronisation regions, and the horizontal solid lines represent the projected regimes from the measurements.

While the effect of mass ratio has been studied for the range of $2.64 \leqslant m^* \leqslant 15.00$ within the capability of the present experimental set-up, future work should investigate the FIV responses with even lower m^* values to answer two particular questions:

- can the 1:1 and 1:3 synchronisation regions interact for $\alpha = 0°$, by increasing the upper U^* bound for the 1:1 mode and decreasing the lower U^* bound for the 1:3 mode?
- does the higher branch associated with sub-harmonic VIV occur for infinite U^* for m^* below a threshold value, as the VIV upper branch of a circular cylinder does?

Acknowledgements

This project has been supported by the Australian Research Council (ARC) Discovery Project (DP) grant DP150103177. In addition, JZ would like to acknowledge the financial support from the ARC grants DP150102879 and DP170100275.

References

Amandolèse, X., Hémon, P., 2010. Vortex-induced vibration of a square cylinder in wind tunnel. Comptes Rendus Méc. 338 (1), 12–17.

Bearman, P.W., 1984. Vortex shedding from oscillating bluff bodies. Annu. Rev. Fluid Mech. 16 (1), 195–222.

Bearman, P.W., Gartshore, I.S., Maull, D., Parkinson, G.V., 1987. Experiments on flow-induced vibration of a square-section cylinder. J. Fluids Struct. 1 (1), 19–34.

Blevins, R.D., 1990. Flow-Induced Vibration, second ed. Krieger Publishing Company, Malabar.

Bokaian, A.R., Geoola, F., 1984. Hydroelastic instabilities of square cylinders. J. Sound Vib. 92 (1), 117–141.

Branković, M., 2004. Vortex-Induced Vibration Attenuation of Circular Cylinders with Low Mass and Damping. Ph.D. thesis, Imperial College London.

Brooks, P.N.H., 1960. Experimental investigation of the aeroelastic instability of bluff two-dimensional cylinders. In: Masters. University of British Columbia.

Carberry, J., Sheridan, J., Rockwell, D., 2001. Force and wake modes of an oscillating cylinder. J. Fluids Struct. 15, 523–532.

Corless, R., Parkinson, G.V., 1988. A model of the combined effects of vortex-induced oscillation and galloping. J. Fluids Struct. 2 (3), 203–220.

Corless, R.M., Parkinson, G.V., 1993. Mathematical modelling of the combined effects of vortex-induced vibration and galloping. Part II. J. Fluids Struct. 7, 825–848.

Den Hartog, J.P., 1932. Transmission line vibration due to sleet. Trans. Am. Inst. Electr. Eng. 51 (4), 1074–1076.

Feng, C.C., 1968. The Measurement of Vortex Induced Effects in Flow Past Stationary and Oscillating Circular and D-Section Cylinders. Master's thesis, The University of British Columbia.

Govardhan, R., Williamson, C.H.K., 2000. Modes of vortex formation and frequency response of a freely vibrating cylinder. J. Fluid Mech. 420, 85–130.

Govardhan, R., Williamson, C.H.K., 2002. Resonance forever: Existence of a critical mass and an infinite regime of resonance in vortex-induced vibration. J. Fluid Mech. 473, 147–166.

Hahn, S.L., 1996. Hilbert Transforms in Signal Processing. Artech House Boston.

Jaiman, R., Guan, M., Miyanawala, T., 2016. Partitioned iterative and dynamic subgrid-scale methods for freely vibrating square-section structures at subcritical Reynolds number. Comput. & Fluids 133, 68–89.

Joly, A., Etienne, S., Pelletier, D., 2012. Galloping of square cylinders in cross-flow at low Reynolds numbers. J. Fluids Struct. 28, 232–243.

Khalak, A., Williamson, C.H.K., 1996. Dynamics of a hydroelastic cylinder with very low mass and damping. J. Fluids Struct. 10 (5), 455–472.

Khalak, A., Williamson, C.H.K., 1997a. Fluid forces and dynamics of a hydroelastic structure with very low mass and damping. J. Fluids Struct. 11 (8), 973–982.

Khalak, A., Williamson, C.H.K., 1997b. Investigation of relative effects of mass and damping in vortex-induced vibration of a circular cylinder. J. Wind Eng. Ind. Aerodyn. 69, 341–350.

Khalak, A., Williamson, C.H.K., 1999. Motions, forces and mode transitions in vortex-induced vibrations at low mass-damping. J. Fluids Struct. 13 (7–8), 813–851.

Klamo, J.T., Leonard, A., Roshko, A., 2005. On the maximum amplitude for a freely vibrating cylinder in cross-flow. J. Fluids Struct. 21 (4), 429–434.

Leontini, J.S., Thompson, M.C., Hourigan, K., 2006. The beginning of branching behaviour of vortex-induced vibration during two-dimensional flow. J. Fluids Struct. 22 (6), 857–864.

Luo, S.C., Bearman, P.W., 1990. Predictions of fluctuating lift on a transversely oscillating square-section cylinder. J. Fluids Struct. 4 (2), 219–228.

Manzoor, S., Hémon, P., Amandolèse, X., 2010. Vortex induced vibrations of a square cylinder in a wind tunnel. In: 3rd Joint US-European Fluids Engineering Summer Meeting. American Society of Mechanical Engineers, pp. 29–34.

Miyanawala, T., Jaiman, R., 2018. Self-sustaining turbulent wake characteristics in fluid–structure interaction of a square cylinder. J. Fluids Struct. 77, 80–101.

Naudascher, E., Rockwell, D., 2005. Flow-Induced Vibrations: An Engineering Guide. Dover Publications.

Nemes, A., Zhao, J., Lo Jacono, D., Sheridan, J., 2012. The interaction between flow-induced vibration mechanisms of a square cylinder with varying angles of attack. J. Fluid Mech. 710, 102.

Païdoussis, M., Price, S., De Langre, E., 2010. Fluid-Structure Interactions: Cross-Flow-Induced Instabilities. Cambridge University Press.

Parkinson, G.V., Smith, J.D., 1964. The square prism as an aeroelastic non-linear oscillator. Quart. J. Mech. Appl. Math. 17 (2), 225.

Ryan, K., Thompson, M.C., Hourigan, K., 2005. Variation in the critical mass ratio of a freely oscillating cylinder as a function of Reynolds number. Phys. Fluids 17 (3), 038106.

Sarpkaya, T., 2004. A critical review of the intrinsic nature of vortex-induced vibrations. J. Fluids Struct. 19 (4), 389–447.

Sen, S., Mittal, S., 2015. Effect of mass ratio on free vibrations of a square cylinder at low Reynolds numbers. J. Fluids Struct. 54, 661–678.

Sen, S., Mittal, S., 2016. Free vibrations of a square cylinder of varying mass ratios. Procedia Eng. 144, 34–42.

Sheikh, N.A., Manzoor, S., Khushnood, S., 2014. A modified non-linear model for high mass ratio square cylinder. J. Mech. Sci. Technol. 28 (12), 4989–4996.

Williamson, C.H.K., Govardhan, R., 2004. Vortex-induced vibration. Annu. Rev. Fluid Mech. 36, 413–455.

Williamson, C.H.K., Roshko, A., 1988. Vortex formation in the wake of an oscillating cylinder. J. Fluids Struct. 2 (4), 355–381.

Wong, K.W.L., Zhao, J., Lo Jacono, D., Thompson, M.C., Sheridan, J., 2017. Experimental investigation of flow-induced vibration of a rotating circular cylinder. J. Fluid Mech. 829, 486–511.

Wong, K.W.L., Zhao, J., Lo Jacono, D., Thompson, M.C., Sheridan, J., 2018. Experimental investigation of flow-induced vibration of a sinusoidally rotating circular cylinder. J. Fluid Mech. 848, 430–466.

Zhao, M., Cheng, L., Zhou, T., 2013. Numerical simulation of vortex-induced vibration of a square cylinder at a low Reynolds number. Phys. Fluids 25 (2), 023603.

Zhao, J., Hourigan, K., Thompson, M.C., 2018a. Flow-induced vibration of D-section cylinders: An afterbody is not essential for vortex-induced vibration. J. Fluid Mech. 851, 317–343.

Zhao, J., Leontini, J.S., Lo Jacono, D., Sheridan, J., 2014a. Chaotic vortex induced vibrations. Phys. Fluids 26 (12), 121702.

Zhao, J., Leontini, J.S., Lo Jacono, D., Sheridan, J., 2014b. Fluid–structure interaction of a square cylinder at different angles of attack. J. Fluid Mech. 747, 688–721.

Zhao, J., Lo Jacono, D., Sheridan, J., Hourigan, K., Thompson, M.C., 2018b. Experimental investigation of in-line flow-induced vibration of a rotating cylinder. J. Fluid Mech. 847, 664–699.

Zhao, J., Nemes, A., Lo Jacono, D., Sheridan, J., 2018c.. Branch/mode competition in the flow-induced vibration of a square cylinder. Philos. Trans. R. Soc. Lond. Ser. A 376, 20170243.